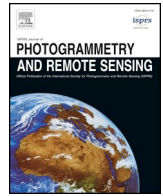


Contents lists available at [ScienceDirect](https://www.sciencedirect.com)

ISPRS Journal of Photogrammetry and Remote Sensing

journal homepage: www.elsevier.com/locate/isprsjprs

Unmanned Aerial System multispectral mapping for low and variable solar irradiance conditions: Potential of tensor decomposition

Sheng Wang^{a,*}, Andreas Baum^b, Pablo J. Zarco-Tejada^{c,d,e}, Carsten Dam-Hansen^f, Anders Thorseth^f, Peter Bauer-Gottwein^a, Filippo Bandini^a, Monica Garcia^{a,g,*}

^a Department of Environmental Engineering, Technical University of Denmark, 2800 Kgs. Lyngby, Denmark

^b Department of Applied Mathematics and Computer Science, Technical University of Denmark, 2800 Kgs. Lyngby, Denmark

^c Department of Infrastructure Engineering, Melbourne School of Engineering, University of Melbourne, Melbourne, Victoria, Australia

^d School of Agriculture and Food, Faculty of Veterinary and Agricultural Sciences, University of Melbourne, Melbourne, Victoria, Australia

^e Instituto de Agricultura Sostenible (IAS), Consejo Superior de Investigaciones Científicas (CSIC), Córdoba, Spain

^f Department of Photonics Engineering, Technical University of Denmark, Denmark

^g International Research Institute for Climate and Society, The Earth Institute, Columbia University, Palisades, NY, USA

ARTICLE INFO

Keywords:

Reflectance

Sensor calibration

Cloud shadow removal

Tucker tensor decomposition

Unmanned Aerial System

ABSTRACT

Unlike satellite earth observation, multispectral images acquired by Unmanned Aerial Systems (UAS) provide great opportunities to monitor land surface conditions also in cloudy or overcast weather conditions. This is especially relevant for high latitudes where overcast and cloudy days are common. However, multispectral imagery acquired by miniaturized UAS sensors under such conditions tend to present low brightness and dynamic ranges, and high noise levels. Additionally, cloud shadows over space (within one image) and time (across images) are frequent in UAS imagery collected under variable irradiance and result in sensor radiance changes unrelated to the biophysical dynamics at the surface. To exploit the potential of UAS for vegetation mapping, this study proposes methods to obtain robust and repeatable reflectance time series under variable and low irradiance conditions. To improve sensor sensitivity to low irradiance, a radiometric pixel-wise calibration was conducted with a six-channel multispectral camera (mini-MCA6, Tetracam) using an integrating sphere simulating the varying low illumination typical of outdoor conditions at 55°N latitude. The sensor sensitivity was increased by using individual settings for independent channels, obtaining higher signal-to-noise ratios compared to the uniform setting for all image channels. To remove cloud shadows, a multivariate statistical procedure, Tucker tensor decomposition, was applied to reconstruct images using a four-way factorization scheme that takes advantage of spatial, spectral and temporal information simultaneously. The comparison between reconstructed (with Tucker) and original images showed an improvement in cloud shadow removal. Outdoor vicarious reflectance validation showed that with these methods, the multispectral imagery can provide reliable reflectance at sunny conditions with root mean square deviations of around 3%. The proposed methods could be useful for operational multispectral mapping with UAS under low and variable irradiance weather conditions as those prevalent in northern latitudes.

1. Introduction

Unmanned Aerial Systems (UAS) have evolved into an important tool in near-Earth observation (Berni et al., 2009; Colomina and Molina, 2014; Manfreda et al., 2018; McCabe et al., 2017; Zarco-Tejada et al., 2012). UAS multispectral mapping brings numerous benefits for environmental monitoring compared to satellites. UAS flying below clouds can provide land surface information under cloudy conditions. This is relevant for high latitude regions where cloudy and overcast

conditions are prevalent (Honkavaara et al., 2012; Wang et al., 2018). Further, UAS multispectral mapping is beneficial for hyper-resolution land surface characterizations to bridge the scale discrepancy between coarse-resolution satellite imagery and field measurements (Fytsilis et al., 2016). This could facilitate to understand the environmental processes and scaling issues at high spatial resolution (Anderson and Gaston, 2013; Wang et al., 2019). Another advantage is that UAS mapping surveys can be conducted with favorable revisit times, flying patterns and low cost. For instance, UAS can serve as a goniometer to

* Corresponding authors at: Department of Environmental Engineering, Technical University of Denmark, 2800 Kgs. Lyngby, Denmark (M. Garcia).
E-mail addresses: shengwang12@gmail.com (S. Wang), mgarc@env.dtu.dk (M. Garcia).

<https://doi.org/10.1016/j.isprsjprs.2019.06.017>

Received 10 January 2019; Received in revised form 25 June 2019; Accepted 26 June 2019

0924-2716/© 2019 International Society for Photogrammetry and Remote Sensing, Inc. (ISPRS). Published by Elsevier B.V. All rights reserved.

study anisotropic effects of the land surface (Von Bueren et al., 2015).

UAS multispectral mapping for scientific research in quantitative remote sensing aims to obtain high spatial and radiometric resolution, high geometric and radiometric accuracy, high dynamic range and low noise level image, high efficiency for data processing and repetitive data acquisition (Honkavaara et al., 2009). Nonetheless, there are challenges in utilizing UAS multispectral mapping for quantitative remote sensing research (Aasen et al., 2018). For instance, UAS platforms are less stable than satellites or manned aerial missions, and imagery from low-cost, consumer-grade multispectral sensors usually has low radiometric resolution and signal-to-noise ratios (SNRs). UAS imagery tends to be more blurry, under or over-exposed and of lower accuracy and repeatability (Von Bueren et al., 2015). Additionally, the low flying height (< 200 m) of UAS results in small coverage of images. To cover the desired survey area, UAS flight campaigns usually acquire hundreds of images during the course of a flight and data processing requires a complex workflow for geometric and radiometric corrections, subsequent orthorectification and mosaicking to generate orthophotos. To solve these issues, studies have designed and improved the workflow on radiometric and geometric processing of UAS multispectral imagery (Aasen et al., 2018; Berni et al., 2009; Del Pozo et al., 2014; Kelcey and Lucieer, 2012; Laliberte et al., 2011). These studies also demonstrated that UAS equipped with low-cost, narrow-band multispectral imaging sensors are able to generate quantitative remote sensing products under sunny and high irradiance conditions, e.g. in the Mediterranean region (Berni et al., 2009; Zarco-Tejada et al., 2012). However, in high latitude regions where the low and variable irradiance conditions are frequent, there are additional challenges to obtain high-quality UAS imagery, including camera sensitivity and cloud shadows in UAS imagery (Honkavaara et al., 2012). Thus, our study aims to improve UAS multispectral mapping under low and variable irradiance conditions.

In high latitude regions such as Denmark, the irradiance is usually low, due to the high frequency of overcast and cloudy days, and low solar height. According to in-situ observations at Soroe eddy covariance site (55°29'N, 11°38'E) of Denmark from 2003 to 2013, only 26.46% of all days at this site are clear (the fraction of diffuse radiation < 50%) as shown in Fig. 1(a). This percentage is lower than the global average (ca. 50%, Kanniah et al., 2012) and the solar irradiance levels on cloudy and overcast days are much lower than that on the sunny days as shown in Fig. 1(b). UAS multispectral imagery obtained in such weather conditions tends to present low brightness and dynamic ranges, and high noise levels. To solve this issue, the multispectral camera should be calibrated with low illumination conditions. This requires cameras to be thoroughly radiometric calibrated and the illumination outputs from the calibration set-up are designed for specific outdoor conditions. Furthermore, to improve the sensitivity, the camera integration time needs to be increased to capture more light. However, at the same time, the too high integration time can induce image saturation. Thus, sensor

settings should fully utilize the radiometric potential of the sensor to avoid over- and under-exposure. Additionally, channels of the multispectral camera may need individual settings of integration times. For instance, vegetation has higher reflectance in the near infrared than in the visible wavelength range. Over vegetated areas, even with low irradiance, saturation can be reached in the near infrared, while visible channels have low brightness. White targets, e.g. snow, can have high reflectance in both visible and near infrared parts. The protocol to identify the optimal sensor setting for individual channels and irradiance conditions needs to be explored to improve sensor sensitivity while preventing saturation (Honkavaara et al., 2012).

Another issue related to the UAS multispectral mapping in high latitude regions is the variable solar irradiance induced by cloud movement during the flight campaign. Even though flight campaigns usually take only 10–20 min, the irradiances of images taken at slightly different times vary due to shading by clouds. This can induce radiometric inconsistency (cloud shadows) across and within images. Numerous studies highlighted the importance of removing cloud shadows for airborne multispectral/hyperspectral data collected on cloudy days (Aasen et al., 2018; Honkavaara et al., 2013; X. Li et al., 2019a; Z. Li et al., 2019b; Zhai et al., 2018). Adeline et al. (2013) categorized cloud shadow detection algorithms into geometric and image based methods including histogram thresholding, invariant color models, object segmentation, geometrical methods, physics-based methods, unsupervised and supervised machine learning methods. Geometric methods based on simulating the radiative transfer processes can potentially achieve a good accuracy. For instance, Brell et al. (2017) used ray tracing methods in combination with return signals of an airborne LiDAR to remove cloud shadows in passive hyperspectral data. However, the geometric method requires accurate geometric information on the 3D objects casting the shadows (clouds in this case), solar elevation and direction, and UAS sensor positions. Due to uncertainties on the geometric information, the accuracy of geometric methods for UAS imagery is relatively low (Aasen et al., 2018; Schläpfer et al., 2012). Using image based methods, Hakala et al. (2013) removed cloud shadows by performing radiance normalization between overlapping areas across images or by collecting the incoming irradiance continuously throughout the entire flight campaign. However, these methods are suitable to remove the radiometric inconsistency across images not within images. Multivariate statistical Tensor decomposition methods have shown to be a useful tool for anomaly detection and removal (Zhang et al., 2016), feature extraction (Zhang et al., 2013) and denoising (Renard et al., 2006) in hyperspectral images. Tensor decomposition is comparable to Principal Component Analysis (PCA), however, differently from PCA, tensor decomposition can deal with the high-dimensional data sets. The Tucker tensor decomposition also has advantages to consider the spatial-temporal patterns simultaneously. The collected overlapping multispectral images or orthophotos across

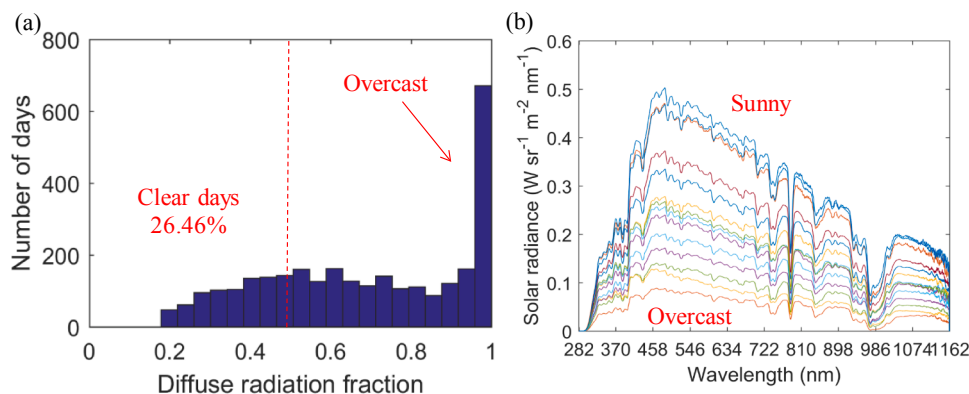


Fig. 1. (a) Observed daily diffuse solar radiation fraction in Soroe of Denmark from 2004 to 2011. (b) Typical solar radiance at 12:00 local time in Risoe, Denmark from July to September 2017.

time from UAS can be treated as a four-way tensor, which has space, spectrum and time dimensions. Using the tensor decomposition, the four-way tensor can be converted into loadings and scores. The obtained loadings can subsequently be used to reconstruct the image with different levels of details in the original image. Depending on how much information is used in the reconstruction, the reconstructed image can contain only the most significant information and exclude noise signals. As the cloud shadow changes with time, the cloud shadow signals can be removed as anomalies from the time domain.

This study is based on the common and established workflow of UAS multispectral image processing (Aasen et al., 2018; Berni et al., 2009; Laliberte et al., 2011). The objectives of this study were: (1) to improve the sensor sensitivity by thoroughly radiometric and geometric calibration of sensors for low irradiance conditions, and (2) to remove the areas of variable irradiance (cloud shadow) on UAS images by tensor decomposition. Finally, the measured reflectance in the field was used to validate the UAS multispectral imagery.

2. Materials

2.1. Multispectral sensor

We use the Tetra mini-MCA camera (MCA, Multispectral Camera Array, Tetracam, Chatsworth, CA, USA), which is one of the most popular multispectral 2D frame imaging sensors for UAS surveys (Bendig et al., 2015; Berni et al., 2009; Laliberte et al., 2011; Turner et al., 2014; Von Bueren et al., 2015; Zarco-Tejada et al., 2012). It has a weight of 700 g, suitable for a lightweight UAS platform. It consists of six independent channels including the visible and near infrared wavelengths. Each channel has a lens in front, a narrow band filter, and a Complementary Metal-Oxide-Semiconductor (CMOS) sensor. Each channel has a field of view of $38.3^\circ \times 31^\circ$ and the focal length is 9.6 mm. The image size is 1280×1024 pixels. The peak wavelengths of the six channels are 470, 530, 570, 670, 710 and 800 nm. The narrow band filters are three-cavity filters, which are characterized by a square peak and steep sideband slopes. The full width at half maximum (FWHM) is around 10 nm. Detailed sensor information is shown in Table 1.

2.2. Laboratory calibration set-up

In order to obtain high-quality UAS imagery, a thorough geometric and radiometric calibration of the MCA was carried out in the laboratory. A standard calibration poster with a checkerboard pattern was used to conduct the geometric calibration and to retrieve the geometric distortion of images. The laboratory radiometric calibration was used to determine the conversion of image digital number (DN) into radiance. The calibration set-up for the radiometric calibration included three parts: a 2 m diameter integrating sphere (ISP2000, Instrument Systems), light sources combining multicolor LEDs (various levels in the visible range) and 3 tungsten halogen lamps (various levels in the near infrared range), and a spectroradiometer (ASD HandHeld 2, Analytical Spectral Devices, Inc., Boulder, Colorado, USA) to record the radiance.

Table 1

Information on the six channels of the MCA camera.

Channel	Color	Central wavelength (nm)	Peak transmission (%)	FWHM (nm)
Slave 1	Blue	470	63.09	467–477
Slave 2	Light green	530	59.72	527–539
Slave 3	Dark green	570	62.99	568–578
Slave 4	Red	670	70.17	666–677
Slave 5	Red edge	710	57.98	706–717
Master	Near infrared	800	59.61	796–806

The integrating sphere is an optical instrument consisting of a hollow spherical cavity with its interior covered with a highly reflective layer of Barium sulfate (BaSO_4). The 2 m diameter integrating sphere ensures multiple diffuse reflections inside the sphere. Thus, uniform and homogeneous illumination is present in the radiance port of the sphere. By changing the electric current going through six multicolor LEDs and three tungsten halogen lamps, this set-up can provide radiance ranging from 0.005 to $0.2 \text{ W}\cdot\text{m}^{-2}\cdot\text{nm}^{-1}\cdot\text{sr}^{-1}$ as shown in Fig. 2(c). This range covers common conditions of reflected radiance in the outside environment. The integrating sphere was set to output 11 illumination levels for sensor calibration based on irradiance levels found in Denmark (Fig. 1). The ASD radiance detector can measure the spectral range from 325 nm to 1075 nm, an accuracy of ± 1 nm and a resolution of < 3 nm at 700 nm. Detailed information on the experimental setup and output spectral radiance are shown in Fig. 2.

2.3. Unmanned Aerial System (UAS)

UAS flight campaigns with an off-the-shelf DJI Hexa-copter Spreading Wings S900 multi-copter platform (DJI S900, DJI Inc., Shenzhen, China) were conducted to deploy the payload to collect imagery at the test site. Besides the MCA multispectral camera, the payload includes an RGB (Red-Green-Blue) camera (Sony DSC-RX100, Corporation, Tokyo, Japan), a GNSS (Global Navigation Satellite System), and a microprocessor Beaglebone Black for sensor communication and data storage. The RGB camera has a focal length of 10.7 mm with a field of view (FOV) of $64.8^\circ \times 45.9^\circ$. A GNSS system (NovAtel flexpak6 and GPS-703-GGG, NovAtel Inc., Canada) (Bandini et al., 2018) was attached with the payload to measure the position information.

3. Methods

A precise geometric and radiometric calibration of the MCA sensor was conducted in the laboratory. After that, the sensitivities of individual channels to radiance were analyzed. An outdoor experiment was conducted over homogeneous targets to test the sensitivities of the individual multispectral channels. Further, the UAS flight campaigns with the MCA camera were conducted under both sunny and cloudy conditions. The digital surface models (DSMs) generated from the MCA images and RGB images were evaluated and compared to assess their geometric accuracy. For the radiometric performance, MCA imagery collected on a variable irradiance (cloudy) day was used to test the cloud shadow removal algorithm. Finally, a vicarious validation of reflectance collected from the UAS orthophotos was performed using reference targets.

3.1. Sensor calibration

The laboratory sensor calibration includes geometric calibration to retrieve lens distortion parameter values, image noise and vignetting correction, and radiometric calibration to link image DN to spectral radiance. The geometric calibration estimated the intrinsic sensor parameters, i.e. the focal length (F), principal point offsets (C_x and C_y), radial distortion coefficients (k_1 , k_2 , and k_3) and tangential distortion coefficients (p_1 and p_2) (Kelcey and Lucieer, 2012). The calibration was conducted using the Brown-Conrady distortion model (Eqs. (1)–(3)) with images taken with a standard checkerboard pattern poster. Radial distortion represents the curving effect generated by the subtle radial shift in magnification towards the center of the lens. Tangential distortion arises from the non-alignment of the lens with the sensor, resulting in a planar shift in the perspective of an image. These pre-calibrated parameter values were used in UAS image processing to correct distortions by warping images with reverse distortions.

$$r = \sqrt{(x - C_x)^2 + (y - C_y)^2} \quad (1)$$

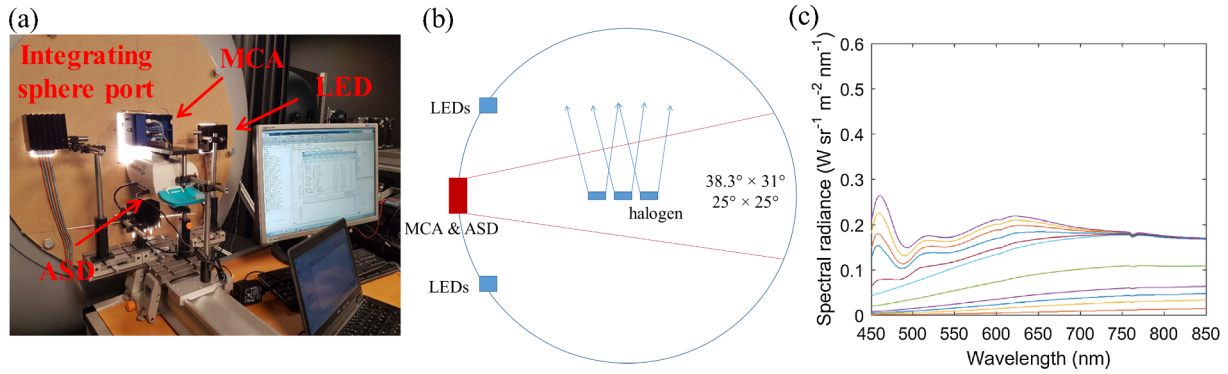


Fig. 2. Laboratory set-up for the radiometric calibration of the 2D frame multispectral sensor. (a) Front view of the set-up including an integrating sphere, an MCA camera, an ASD spectroradiometer and LED light sources. (b) The top cross section view of the set-up. The bottom of the integrating sphere is halogen light sources. The numbers indicate the field of view of MCA ($38.3^\circ \times 31^\circ$) and ASD ($25^\circ \times 25^\circ$). (c) Spectral radiance at the port of the integrating sphere measured by the ASD. The curves with different colors represent different illumination intensities. These spectral intensities of light sources approximately cover the most reflected radiance conditions in the outdoor environment (The typical solar spectral radiance is shown in Fig. 1).

$$\begin{aligned} x' &= x(1 + k_1r^2 + k_2r^4 + k_3r^6 + k_4r^8) + (P_1(r^2 + 2x^2) + 2P_2xy) \\ &\quad (1 + P_3r^2 + P_4r^4) \end{aligned} \quad (2)$$

$$\begin{aligned} y' &= y(1 + k_1r^2 + k_2r^4 + k_3r^6 + k_4r^8) + (P_2(r^2 + 2y^2) + 2P_1xy) \\ &\quad (1 + P_3r^2 + P_4r^4) \end{aligned} \quad (3)$$

where x' and y' are distorted image point on the projected image plane. r is the distortion displacement distance from the principal point. x and y are the coordinates in the undistorted image projection. C_x and C_y are principal point offset. k_1 , k_2 and k_3 are radial distortion coefficients. p_1 and p_2 are tangential distortion coefficients.

The radiometric calibration of the MCA included three steps: noise removal, vignetting correction and converting the image DN to radiance. The dark current noise, which represents the image DN in the absence of light and has consistent values and patterns, is a major source of sensor noise (Del Pozo et al., 2014). The dark current noise can be evaluated in the laboratory without light.

Vignetting effects refer to higher DN values in the center of images than towards the edges under homogeneous illumination. This is due to the higher light incidence angle in the center of images than that in the edges. Additionally, the optical lens can distort the light paths and more light reaches the center. The vignetting effects could be removed by using the camera to take images of a Lambertian plate (Spectralon or Teflon panels) under homogeneous illumination conditions (e.g. Kelcey and Lucieer, 2012). This method is quite easy to be implemented, but in practice, due to the wide-angle lenses, it can be hard to have the sensor FOV completely within the reference target while getting homogeneous illumination (Yu, 2004). Another practical method is using non-perfect targets but averaging thousands of images to reduce noise (e.g. Von Bueren et al., 2015). For instance, Hakala et al. (2010) averaged images with a snow background to remove vignetting. Single image based vignetting removal algorithms (e.g. Zheng et al., 2013), which are based on the symmetry of the vignetting noise, are another possible approach (Schirrmann et al., 2016). An integrating sphere can provide homogeneous illumination and images with the integrating sphere can also be used to quantify the vignetting effects (Yu, 2004).

The final step of radiometric calibration is converting the image DN to the physically meaningful unit, radiance. Images with the integrating sphere at different illumination levels and integration times were used. A linear model as Eq. (4) (Ferrero et al., 2006) was adopted in this study to link DN with spectral radiance. Different from previous studies (Kelcey and Lucieer, 2012) to conduct radiometric calibration with several consecutive steps, we performed a pixel-wise calibration to remove dark noise and vignetting effects, and transfer DN to spectral

radiance simultaneously. By combining Eq. (4) and (5), we can obtain Eq. (6) for the pixel-wise calibration. The image pixel-wise values of three parameters (a , b and DN_{dark}) were obtained by fitting dark current images and images taken with the integrating sphere with different radiance levels and integration times.

$$L = c_1 \cdot DN + c_0 \quad (4)$$

$$c_1 = a \cdot t^b \quad (5)$$

$$L = a \cdot t^b \cdot (DN - DN_{\text{dark}}) \quad (6)$$

where L denotes the spectral radiance ($\text{W} \cdot \text{m}^{-2} \cdot \text{sr}^{-1} \cdot \text{nm}^{-1}$). c_1 is the spectral gain, which normally has a power law relationship with integration time t ($\text{W} \cdot \text{m}^{-2} \cdot \text{sr}^{-1} \cdot \text{nm}^{-1}$). c_0 is an offset ($\text{W} \cdot \text{m}^{-2} \cdot \text{sr}^{-1} \cdot \text{nm}^{-1}$), which represents an offset to correct the dark current (DN_{dark}). DN denotes Digital number of the image pixels (no unit). L stands for the spectral radiance of the illumination from the integrating sphere, which is measured by ASD. The fitting parameters a ($\text{W} \cdot \text{m}^{-2} \cdot \text{sr}^{-1} \cdot \text{nm}^{-1} \cdot \text{ms}^{-1}$) and b (no unit) are empirical coefficients and need to be estimated.

For simplicity, this study used the pixel-wise calibration to integrate these three steps, the noise removal, vignetting correction and converting the image DN to radiance, into one step using Eq. (6). The images taken with the integrating sphere of a 2-m diameter were used to determine dark noise, vignetting and linking DN to spectral radiance. For each integration time setting and each illumination level, 30 images were taken with the integrating sphere and then the averaged values were used for calibration. The integration times were set to from 1 to 8 ms with 1 ms increment and the illumination intensities were set to 11 levels to cover the most prevalent conditions of reflected radiance in the outside environment. The integration times from 5 to 8 ms were designed for low illumination in high-latitudes, while typically in mid-latitudes, integration times up to 4 ms were sufficient (Berni et al., 2009).

3.2. Sensitivity of individual sensor channels

As the spectral gain c_1 in Eq. (4) represents the linkage between DN and radiance, c_1 with a large value indicates that the sensor channel can have a high sensitivity to the light intensity. Whereas, a relatively small value of c_1 shows that the sensor channel has a low sensitivity to the light intensity. Thus, we analyzed the relationship between the averaged spectral gains of the entire image with various integration times. The comparison of the spectral gains can show the sensitivity of individual channels to the light intensity. Furthermore, it provides insights into the optimal setting of the integration time to maximize the image SNR, which is the ratio between the averaged image signal

($DN - DN_{\text{dark}}$) and the averaged image dark noise (DN_{dark}). That means under a certain level of light intensity, the camera setting of the integration times should keep image SNR highest while preventing image DN saturation.

To test the sensitivity of individual channels with various targets in the field condition, an outdoor experiment was conducted with homogenous experimental plots, i.e. Teflon, grass and bare soil plots. Teflon has a high reflectance in both the visible and near infrared, and it is similar to snow. Grass has a relatively high reflectance in the near infrared and a low reflectance in the visible part, while soil has a relatively high reflectance in the visible and low reflectance in the near infrared. Images were taken on 6th January 2017, which was an overcast and low irradiance day (around $0.1 \text{ W}\cdot\text{m}^{-2}\cdot\text{sr}^{-1}\cdot\text{nm}^{-1}$). The sensor integration time was set to five levels (1, 4, 8, 12 and 16 ms). The SNRs were calculated for the MCA images with different integration times to identify the relationship between the SNRs and the integration time settings. In order to avoid BRDF effects, MCA was kept as orthogonal to the targets as possible. For each experimental plot, 30 images have been taken with each integration time setting. To reduce uncertainties, these 30 images were averaged to evaluate the responses of SNRs to the integration times.

3.3. Flight campaigns

UAS flight campaigns were conducted at an eddy covariance flux site (DK-RCW) in Risoe, Roskilde, Denmark. This site is an 11-ha willow bioenergy plantation ($55^{\circ}41'31.95''\text{N}$, $12^{\circ}6'14.69''\text{E}$). The eddy covariance tower in the field recorded the meteorological conditions during the flight campaigns. Flight paths (Fig. 3) were designed using the DJI autopilot software. The imagery was acquired by UAS with a horizontal speed of $3 \text{ m}\cdot\text{s}^{-1}$ resulting in 60% forward and 40% side overlapping. The flight campaigns were conducted on four different days. The first campaign was to validate the accuracy of DSMs generated from MCA and RGB images. The other three campaigns (two cloud-free days and one cloudy day) were mainly used to validate the reflectance obtained from UAS. Details on these flights are shown in Table 2. Two flights were conducted during partially cloudy weather conditions to deal with the inconsistency of reflectance across multispectral images and test the cloud shadow removal algorithm.

To improve the geometric accuracy of image processing, the Trimble RTK GNSS R8s (Trimble Inc., Sunnyvale, CA, USA) with an accuracy of 8 mm (horizontal) and 15 mm (vertical) was used to measure ground control points (GCPs) after the UAS flight campaign. An ASD spectroradiometer was used to measure the reflected radiance and reflectance over the Spectralon panel and portable tarpaulins. The Spectralon panel reflects 99% of incoming solar irradiance, thus we used ASD to measure the reflected radiance from Spectralon to calculate reflectance for MCA. Each target was measured by ASD 20 times before and after the flights and the averaged values from these 40 measurements were used as the incoming solar radiance.

3.4. Digital surface model and orthomosaic generation

The raw MCA images were firstly converted to tiff format and the 6 bands were aligned using the Pixelwrench2 software (Tetracam, California, USA). Then, the pixel-wise radiometric correction was applied to remove dark current and vignetting, and to convert DN to radiance. After that, images were imported into Agisoft Photoscan (Agisoft LLC, St. Petersburg, Russia) to conduct the Brown-Conrady geometric correction with pre-calibrated parameter values. Agisoft is an image mosaicking software based on the structure-from-motion method (SfM), which solves the camera position and orientation by the bundle adjustment based on feature matching between image overlapping (Westoby et al., 2012). It is an inexpensive, effective and flexible approach to process UAS images (Aasen et al., 2018). Detailed workflow on aerial triangulation, digital surface model and orthomosaic generation in Agisoft is shown in Fig. 4.

Aerial triangulation determines the orientation of each stereo model in an image block. The exterior position parameters of each image from the GNSS were firstly used to aid the image alignment process. Then, the pre-calibrated geometric parameter values of MCA (i.e. focal length, principal point, and distortion coefficients) were imported to Agisoft. Further, the image process was performed by bundle adjustment in Agisoft, which allowed the absolute orientation of an entire image block using limited GCPs (Abe et al., 2010). To compute the aerial triangulation, tie points were automatically detected in pairs of single overlapping images by the Scale Invariant Feature Transform (SIFT) algorithm (Lowe, 2004). Compared to MCA images, RGB images have

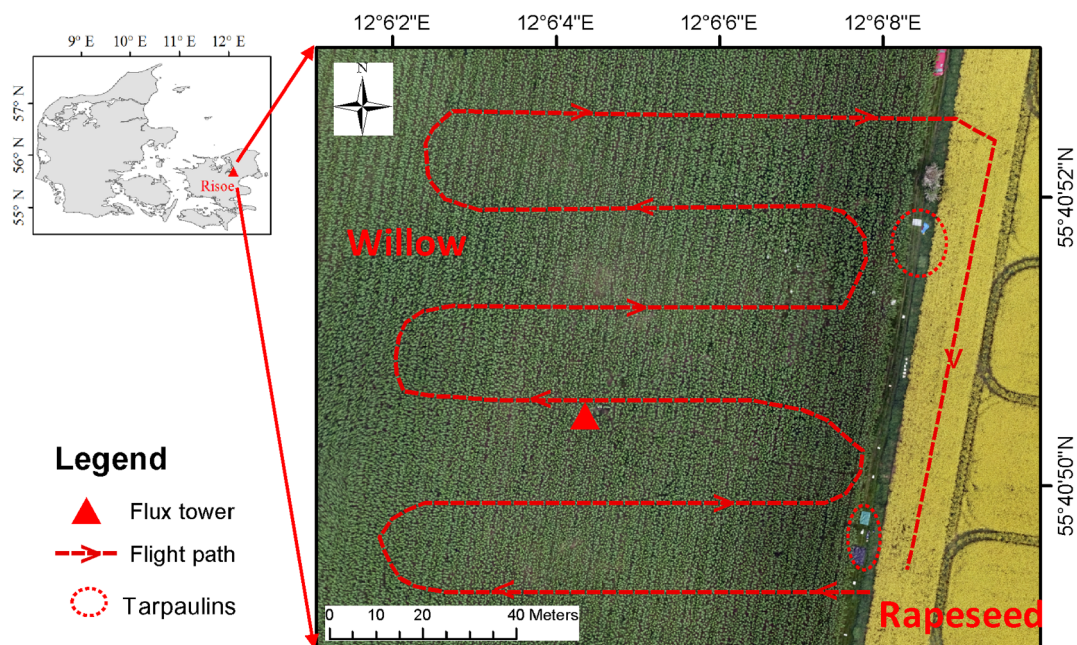


Fig. 3. Overview of the Risoe study site and the flight path of UAS campaigns. The flux tower is in the middle of the willow plantation. The dashed line indicates the flight pattern. Four color reference tarpaulins are inside the dotted circles.

Table 2

Information on the flight campaigns (RH: relative humidity; WS: wind speed at 10 m; Pa: air pressure; Solar Irrad.: solar irradiance; Std: standard deviation over time of flight; GSD: ground sampling distance). *Two flights (one flight in a sunny moment and one flight in a cloudy moment).

Date	Acquisition time	Weather	RH (%)	Ta (°C)	WS (m·s ⁻¹)	Pa (kPa)	Solar Irrad. (W·m ⁻²)	Std of solar Irrad. (W·m ⁻²)	Flying height (m)	GSD (m)
25-May-2016	10:11–10:23	Sunny	62.67	21.05	3.30	100.89	744.26	3.22	12	0.01
19-May-2017	12:07–12:19	Sunny	79.25	19.27	2.13	101.41	792.03	2.16	90	0.05
26-May-2017	11:13–11:26	Sunny	72.56	16.72	4.47	101.54	823.17	2.16	90	0.05
18-Jun-2017*	12:25–12:51	Cloudy	71.79	21.81	4.42	101.62	848.77	18.18	90	0.05

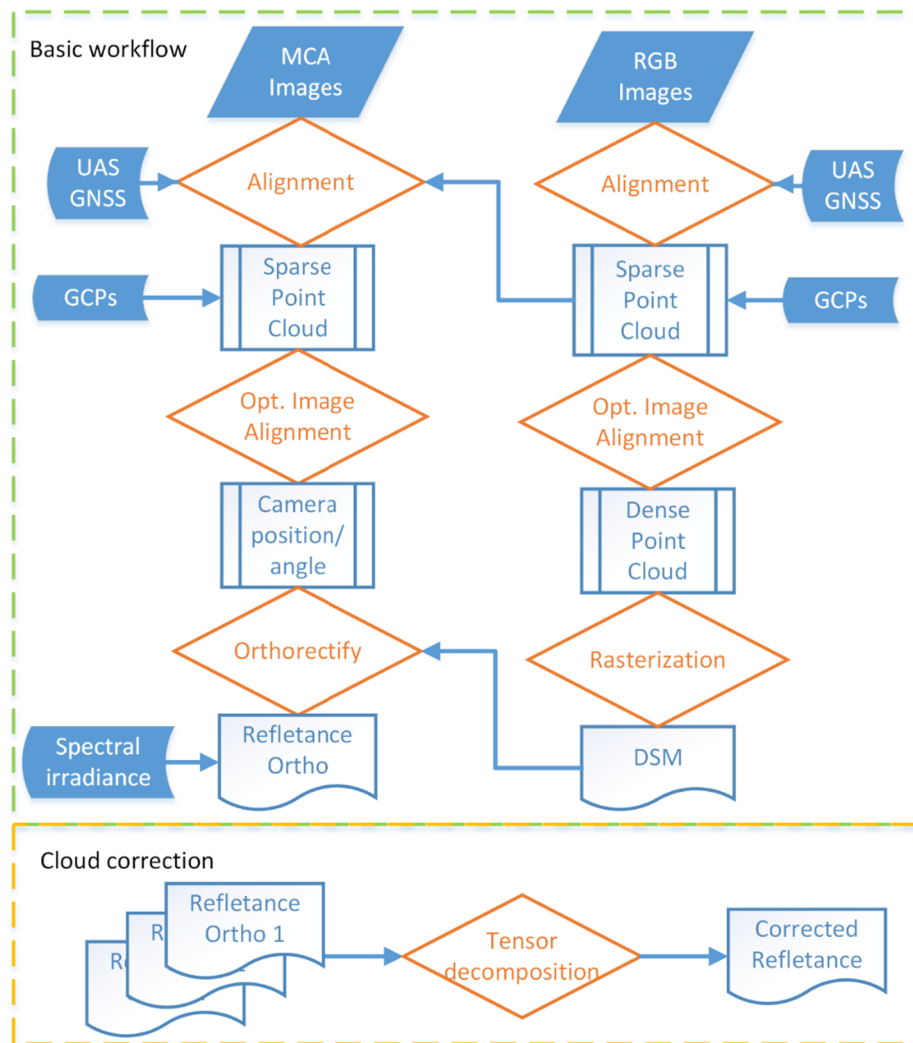


Fig. 4. Flowchart for UAS image processing. The basic workflow is to process MCA images collected under sunny conditions, while in the cloudy conditions with variable irradiance, additional processes in the orange box need to be conducted. GCP: ground control points. Opt. Image Alignment: optimizing image alignment. DSM: digital surface model. Orthos: orthophotos. (For interpretation of the references to color in this figure legend, the reader is referred to the web version of this article.)

larger FOV and higher radiometric resolution. Feature points in RGB images can be more easily identified and linked to MCA images. Thus, the sparse point clouds from RGB images were added to the MCA project to improve the image alignment. After that, the GCPs from the Trimble GNSS were manually identified and added to the target survey area to improve the triangulation process.

The DSM can be produced by rasterizing the dense point cloud generated from the aerial triangulation. However, compared to the RGB camera, the MCA camera cannot generate DSMs with high accuracy due to a narrow FOV, small image size, and low geometric camera performance. Additionally, the MCA camera is a rolling shutter sensor and pixels in images are not all exposed simultaneously, although Agisoft

takes the rolling shutter effect into account (Mesas-Carrascosa et al., 2017). To validate DSMs generated by MCA and RGB images, the Trimble GNSS was used to randomly measure surface elevation in the study site on 25th May 2016. The two DSMs from MCA and RGB images were generated with the same GNSS data onboard, GCPs and processing procedures. This comparison can provide insights into the suitable camera for DSM generation to further orthorectify MCA images.

In the final stage, each image was orthorectified according to the external orientation (position and orientation) and the DSM. Then individual orthorectified images were combined into a seamless six-band multispectral orthomosaicked orthophoto for the entire area. Finally, the six band reflectance was generated from the multispectral

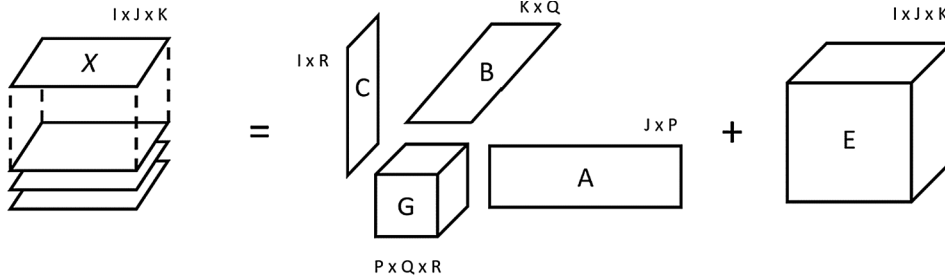


Fig. 5. A three-way tensor, with two spatial modes with $J \times K$ pixels and one temporal mode with I orthophotos, can be decomposed into loadings A , B and C and a core tensor G using the Tucker tensor decomposition method, where E represents the residuals or error matrix ideally. Depending on the chosen number of components for each mode (P , Q and R), the original data can be reconstructed to produce orthophotos without artifacts (such as cloud shadows) and noise. Ideally, artifacts and noise represent the major variance in the residuals E and all systematic spatial-temporal information is re-constructed from A , B , C and G .

orthophotos based on the radiance method, which is more accurate than the empirical line method (Biggar et al., 1994; Del Pozo et al., 2014). In the radiance-based method, the reflected spectral radiance for each band ($L_{MCA,\lambda}$) was measured by the MCA, while a spectral radiometer ASD was used to collect the incoming solar spectral radiance over a Spectralon panel (nominal reflectance of 99.99%) before and after each UAS flight campaign. Due to the short duration of the flight (around 12 min), the averaged ASD measurements before and after each flight was used to represent the incoming radiance for each flight. Due to different spectral resolutions of MCA and ASD, the solar spectral radiance from ASD was convoluted to $L_{in,\lambda}$ using the MCA filter transmissivity. Further, six-band reflectance was calculated as Eq. (7). To deal with the cloud shadow issue, the tensor decomposition method was further applied to remove cloud shadows in the orthophotos of reflectance, as shown in the flowchart in Fig. 4.

$$\rho_{MCA,\lambda} = \frac{L_{MCA,\lambda}}{L_{in,\lambda}} \quad (7)$$

where λ is the wavelength (nm). $\rho_{MCA,\lambda}$ is the reflectance for the wavelength λ . $L_{MCA,\lambda}$ is the reflected spectral radiance measured by MCA ($W \cdot m^{-2} \cdot sr^{-1} \cdot nm^{-1}$). $L_{in,\lambda}$ is the incoming spectral radiance measured by ASD ($W \cdot m^{-2} \cdot sr^{-1} \cdot nm^{-1}$).

3.5. Cloud shadow correction using tensor decomposition

Tensor decomposition methods are typically employed when data are measured in more than two dimensions, hence its data structure can be represented as organized in “boxes” rather than matrices (Mørup, 2011). These boxes are referred to as tensors and its dimensions are called modes. In this study, each orthophoto has J pixel rows and K pixel columns. These I orthophotos of the same area can be stacked to form a three-way tensor as shown in Fig. 5. In this tensor, each pixel can be identified using the indices i , j and k , which correspond to the acquisition time point, pixel row and column, respectively. An illustration for a Tucker decomposition of stacked orthophotos (the spectral dimension is not considered) is illustrated in Fig. 5. The decomposition yields loading matrices A , B and C and a core tensor G . A and B

represent loading matrices for the pixel row and column mode, respectively, and C represents the loading for the temporal mode. The dimensionality of G and the loading matrices A , B and C depend on the chosen number of components in each mode. While P and Q indicate the number of components for the pixel row and column modes, R indicates the number of components for the temporal mode. To remove cloud shadows, R is chosen to be small, e.g. 1. On the other hand, P and Q are chosen to be large, e.g. 100, to allow for sufficient image resolution of the desired reconstruction. The reason for choosing R to be small, e.g. 1, is due to the assumption of low rank in the temporal mode, meaning that one can expect all pixels to co-change over time in a similar manner. After the tensor decomposition, the orthophotos can be reconstructed using the loadings and core tensor. The residuals E contain an unexplained variation of the model, which is ideally due to the cloud shadows and noise.

To show the potential of the tensor decomposition for cloud shadow removal, this study used three multispectral images acquired from UAS at slightly different time on 18th June 2017 to stack into a four-way tensor (two dimensions in space, one dimension in time and one dimension in wavelength). Because it is difficult to illustrate such four-way data, we chose to illustrate the decomposition using a three-way tensor with the spectral dimension (Fig. 5). However, the four-way Tucker decomposition can be formalized elementwise as shown in Eq. (8). Matrix and tensor elements are represented with the lower-case letters of the corresponding tensor X , loadings A , B and C and a core tensor G in Fig. 5. Hence, $x_{i,j,k,l}$ represents a pixel value at a given time point i , row number j , column number k and wavelength l . Elements of the spectral mode loading D are denoted as $d_{l,s}$, where l and s represent wavelength and spectral mode component indices.

$$x_{i,j,k,l} = \sum_{p=1}^P \sum_{q=1}^Q \sum_{r=1}^R \sum_{s=1}^S g_{p,q,r,s} \cdot a_{i,p} \cdot b_{j,q} \cdot c_{k,r} \cdot d_{l,s} + e_{i,j,k,l} \quad (8)$$

3.6. Vicarious reflectance validation

To validate the accuracy of the reflectance, the averaged reflectance of 20 measurements from tarpaulins (green, blue, black and silver) was used to validate the estimated reflectance from the MCA in sunny

Table 3

Calibrated geometric parameter values of the MCA and RGB cameras. The first column is the parameters, e.g. focal length (F), principal point offsets (C_x and C_y), radial distortion coefficients (k_1 , k_2 , and k_3) and tangential distortion coefficients (p_1 and p_2). The second to seventh columns are the calibrated parameter values for MCA and the last column shows the calibrated parameter values for the RGB camera.

Parameter (mm)	800 nm	470 nm	530 nm	570 nm	670 nm	710 nm	RGB
F	9.89E+00	9.89E+00	9.81E+00	9.89E+00	9.75E+00	9.82E+00	2.83E+01
C_x	-1.74E-01	-2.61E-01	6.38E-01	5.92E-03	7.64E-01	2.81E-01	2.20E-02
C_y	1.17E-01	-6.69E-01	-5.12E-01	-4.06E-01	-1.01E+00	-6.66E-01	-7.40E-02
k_1	-1.75E-03	-1.83E-03	-8.15E-04	-1.22E-03	6.09E-05	-7.72E-04	1.41E-05
k_2	1.30E-02	1.25E-02	4.90E-03	5.08E-03	-3.44E-03	3.64E-03	-1.83E-07
k_3	-4.48E-02	-4.01E-02	-1.34E-02	-1.29E-02	5.94E-03	-1.22E-02	-2.21E-10
p_1	2.76E-05	8.54E-06	3.52E-05	2.72E-05	3.58E-05	2.54E-05	1.00E-12
p_2	1.41E-05	-3.71E-05	-3.20E-05	-5.22E-05	-3.72E-05	-4.54E-05	1.00E-15

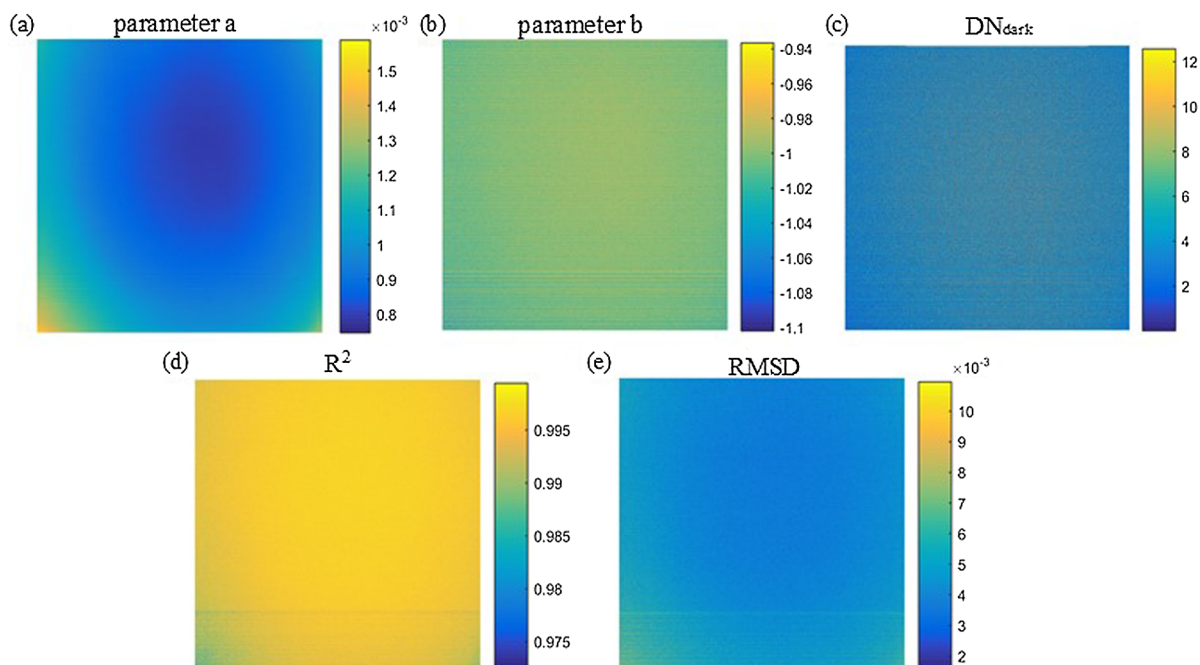


Fig. 6. (a–c) Values of the calibrated parameter a ($\text{W}\cdot\text{m}^{-2}\cdot\text{sr}^{-1}\cdot\text{nm}^{-1}\cdot\text{ms}^{-1}$), b (no unit), DN_{dark} (no unit). (d–e) R^2 and RMSD [$\text{W}\cdot\text{m}^{-2}\cdot\text{sr}^{-1}\cdot\text{nm}^{-1}$] for the pixel-wise calibration approach. Only results of the master channel (800 nm) are shown and results of other channels are shown in supplemental Fig. S1.

conditions. Tarpaulins are acknowledged to have low anisotropy effects (Korpela et al., 2011). The reflectance measured with ASD was used as ground truth to validate reflectance from MCA. Statistics such as root mean square deviation (RMSD), bias and correlation coefficient (R) were used to evaluate the quality of the estimated reflectance from MCA imagery. We assume that atmospheric effects on the radiance are negligible ($< 1\%$) due to the low flight altitude (90 m) (Yu et al., 2016).

4. Results and discussion

4.1. Sensor calibration

The calibrated geometric parameter values of MCA and RGB cameras are shown in Table 3. These calibration results are similar to other studies on the geometric calibration of MCA (Kelcey and Lucieer, 2012). The comparison between geometric calibration parameter values of MCA and those of RGB cameras, e.g. principal point offsets, confirms the more precise geometric configuration of the RGB camera. This supports to use the RGB images to generate the accurate DSM to further orthorectify MCA images.

The parameter values of the pixel-wise radiometric calibration, a, b and DN_{dark} (Eq. (4)) are shown in Fig. 6(a–c). Here only results for the calibration of the master channel (800 nm) are shown in Fig. 6. It can be seen that the matrix of parameter a (Fig. 6a) shows lower values in the middle, while the higher values are on the edge which allows correcting for the vignetting effects. The spatial pattern of parameter b, which links the integration times with radiance, is more uniform. DN_{dark} is about 1% of the radiometric resolution of MCA (10 bit, 1024). The calibration performance, R^2 and RMSD, is also shown in Fig. 6(d–e). The high values of R^2 and the low values of RMSD show that this calibration model (Eq. (4)) could well represent the radiometric response of this sensor and the pixel-wise calibration method is valid for sensor radiometric calibration. Calibration results for other channels are similar to the results of 800 nm. Details can be found in supplemental Fig. S1.

4.2. Sensitivity of individual sensor channels

The sensitivity of individual channels to the radiance is shown in Fig. 7. It can be seen that with the same levels of integration times, the 470 and 800 nm channels have the highest gains (parameter c_1), while the 670 nm channel has the lowest gain. This suggests that 670 nm is the most sensitive channel to radiation changes, while the 470 nm and 800 nm channels are least sensitive to the radiation change. The sensitivity of each channel is determined by the peak transmission of filters (Table 1) and the spectral sensitivity of the CMOS sensor. The 670 nm channel has both the highest filter peak transmission and CMOS sensitivity, while the CMOS sensor has the lowest sensitivity to the 470 nm and 800 nm channels (Del Pozo et al., 2014). The analysis of spectral gains implies that as different MCA channels have different sensitivities, these channels may need individual settings of integration times in order to obtain images with the best quality.

Fig. 8 shows the experimentally determined SNRs for different settings of integration times and three surface types (Teflon, grass and soil). As shown in Fig. 8(a), the image SNRs increased with larger

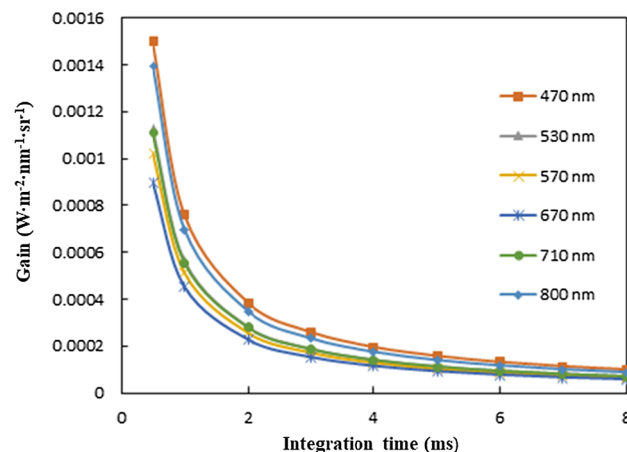


Fig. 7. Gains (parameter c_1) for each channel with integration time from 0.5 to 8 ms.

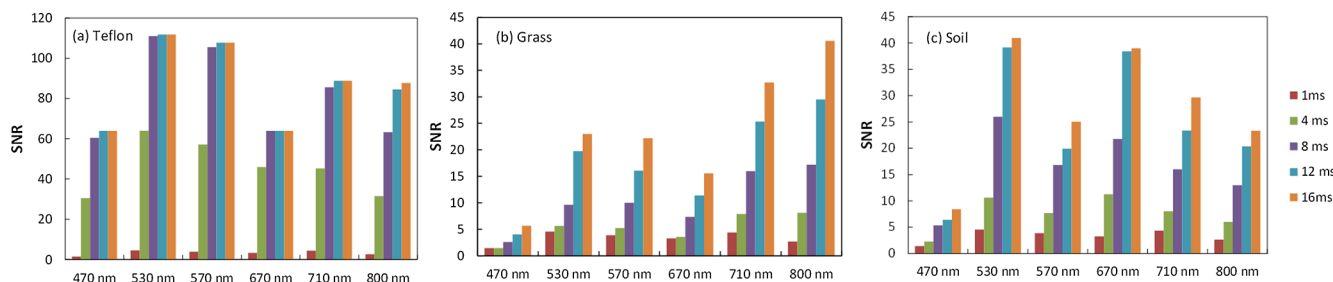


Fig. 8. Signal-to-noise ratio (SNR) for different integration time settings and targets (a: Teflon, b: Grass, c: Soil) under constant illumination for low conditions (The irradiance is around $0.1 \text{ W}\cdot\text{m}^{-2}\cdot\text{sr}^{-1}\cdot\text{nm}^{-1}$). The x-axis is the different channels and the y-axis is the image SNR.

integration times. However, after a certain level (approximately $\text{SNR} = 60$ for 470 and 670 nm, $\text{SNR} = 110$ for 530 and 570 nm, $\text{SNR} = 80$ for 710 and 800 nm), the image SNRs do not change due to the saturation of image DNs. The maximum SNR levels for different channels relate to the dark noise level of each channel. In practical applications, the optimal integration time settings should maximize the image SNRs while avoiding image saturation. This means that in this case of very low irradiance conditions ($0.1 \text{ W}\cdot\text{m}^{-2}\cdot\text{sr}^{-1}\cdot\text{nm}^{-1}$) and low reflectivity land covers such as grass or soil, the optimum integration time will coincide with the maximum integration time. However, for the high reflectivity target, Teflon, even with low irradiance values saturation is reached after 8 ms, so the optimum integration time, in this case, will be 4 ms for bands 530 to 710 nm and 8 ms for 470 and 800 nm. The larger integration times for 470 and 800 nm channels agree with Fig. 6, which indicates the low sensitivity of 470 and 800 nm channels.

By comparing different targets (land cover types) in Fig. 8, it can be seen that different settings of integration times are needed for individual channels. For the case of Teflon (similar to snow), the optimum integration time will be 4 ms for bands 530–710 nm and 8 ms for 470 and 800 nm. Therefore, if a uniform integration time (4 ms) is used for all channels, the SNRs for the 470 and 800 nm would be 30 and 32, respectively. However, if we use the integration time of 8 ms, the SNRs would be about 60 and 62, respectively. In this way, we can see the benefits of using different settings rather than the uniform setting for all channels. For grass, with the same levels of integration times, the near infrared and red edge (800 and 710 nm) have a higher SNR. For soil, with the same levels of integration times, the 530 and 670 nm have a higher SNR. These findings indicate that the setting of the integration time should be set with individual channels and different land surface conditions. For instance, to monitor vegetation, the integration time settings of the near infrared and red edge should be smaller than those of the visible bands. Similarly, the integration time of the near infrared for soil may be larger than that of some visible bands.

To further optimize the sensitivity of each channel under different illumination and land surface conditions, several approaches can be used. The first approach could be to use the prior knowledge of the reflected radiance to determine the optimal integration time for each channel. As thoroughly laboratory radiometric calibration has been conducted, the relationship between image DN and radiance is known. Thus, with the prior knowledge on how much radiance is reflected from the surface, the radiometric calibration model of the camera (Eq. (6)) could be inverted to get the optimal integration time. To obtain the reflected radiance from the surface, one can possibly use a spectroradiometer to measure the reflected radiation before the flights. An example is the willow plantation is the mapping target in this study. We can use a field spectroradiometer (e.g. ASD) to measure the reflected radiance of an accessible vegetation target before the flight. Then this information can be used to determine the optimal integration time for the MCA camera. One challenge of this approach is in the case of highly variable solar irradiance and conditions when collecting spectroradiometer measurements could be different from the conditions when conducting flight campaigns. To account for that, another approach would be to install a spectroradiometer with a cosine receptor on the UAS (Hakala et al., 2013). By collecting solar radiance continuously and with the prior knowledge on the reflectance of mapping targets, the camera can automatically adjust the optimal setting of integration time for different MCA channels. Additionally, another approach for optimizing the image SNRs would be to determine the image integration time setting based on the quality in terms of saturation and dynamic ranges of the previous image. For instance, based on the histogram of the previously collected image, one could adjust the integration time settings for the next frame.

4.3. Digital surface model and orthomosaic

Fig. 9 shows the DSM generated by RGB and MCA images on 25th May 2016 and their validation results. It can be seen the DSM from RGB

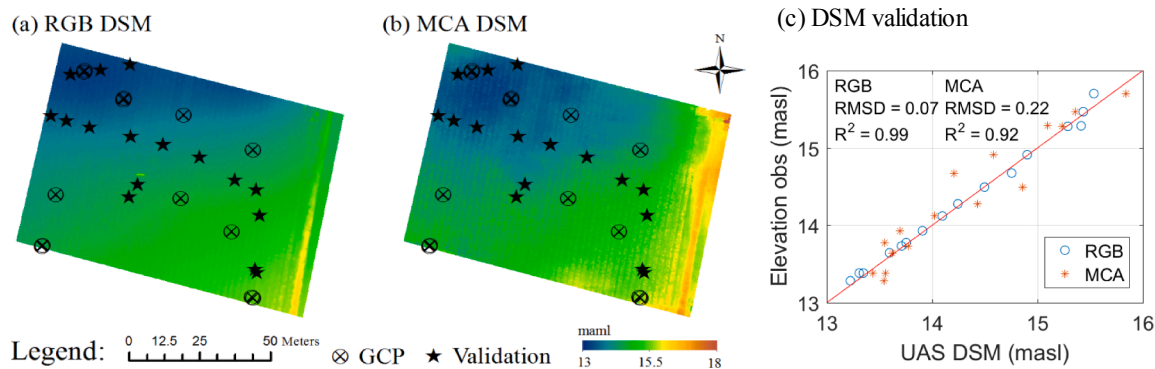


Fig. 9. Comparison of the DSM generated from the RGB and MCA cameras. Ground control points (GCP) were used as inputs of the Agisoft image processing. The validation points were independent measurements to check the accuracy of the DSMs generated from RGB and MCA camera. (a) is the DSM from RGB images. (b) is the DSM from the MCA images. (c) is the validation of the DSM generated from RGB and MCA images.

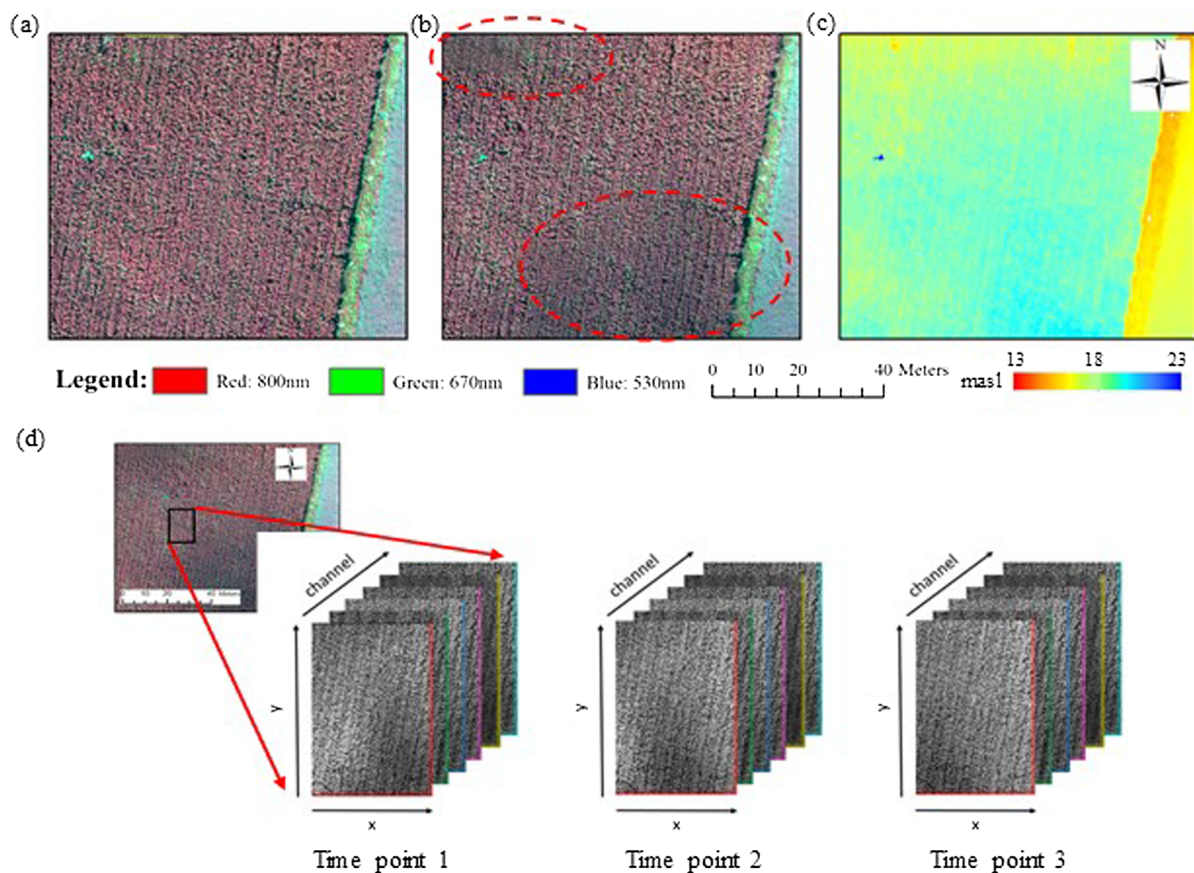


Fig. 10. Pseudo-color multispectral orthophotos generated from UAS multispectral images. The red, green and blue channels correspond to 800, 670 and 530 nm. (a) is the orthophoto without cloud shadow. (b) is the orthophoto with cloud shadow and the red circles indicate the cloud shadow. (c) is the digital surface model (DSM) generated from RGB images and is used for the orthorectification of multispectral images. (d) is to illustrate using the orthorectified UAS images to test the cloud shadow removal algorithms. The data cubic for the tensor decomposition is a four-way tensor (two dimensions in space, one dimension in the spectral domain and one dimension in the temporal domain). (For interpretation of the references to color in this figure legend, the reader is referred to the web version of this article.)

and MCA images have similar spatial patterns, lower elevation in the upper left corner and higher elevation in the right bottom corner. Fig. 9(c) shows using the independent Trimble RTK GNSS measurements to validate the generated DSM. It can be found that the DSM from RGB images has a higher accuracy with RMSD of 0.07 m and R^2 of 0.99, while the DSM from MCA images has a lower accuracy with RMSD of 0.22 m and R^2 of 0.92. This supports the results of Table 3 and indicates RGB images are more suitable for DSM generation than MCA images.

Fig. 10 shows the pseudo-color multispectral orthophotos during cloudy weather conditions (18th June 2017). Fig. 10(a) is the orthophoto generated from images collected during sunny conditions, while (b) is the orthophoto generated from images collected under the variable irradiance conditions. In Fig. 10(b), the darker areas in the left upper corner and right bottom corner are not related to the vegetation growth but to cloud shadows. Fig. 10(c) is the generated DSM from RGB images. To test the cloud shadow correction, the orthorectified images from Fig. 10(b) were used as shown in Fig. 10(d). These three pairs of images collected at slightly different times and show the movement of the cloud shadow from the right bottom corner to the left bottom corner. These images were used as a four-way tensor to test the cloud shadow correction method.

4.4. Cloud shadow correction

Fig. 11 shows the results on the Tensor decomposition to correct the cloud shadow in reflectance from the example of Fig. 10. It can be seen that in the original images, the shadow was in the left bottom corner of the image at the time point 1. At the time point 2, the shadow was at the

middle bottom of the image, while at the time point 3, the shadow was at the left bottom corner of the images. With the tensor decomposition, the cloud shadow was successfully removed as shown in the reconstructed image of Fig. 11. In the residual (the reconstructed image minus the original image), we can find the higher values in the left bottom corner, which corresponds to the location of the cloud shadow. More reconstructed and residual images can be found in supplemental Fig. S2. The comparison of the pseudo-color images is shown in Fig. supplemental S3.

In this study, the signal changes in the time domain were used to remove the cloud shadow. This means that P, Q and S in Eq. (8) were chosen to be large to allow for sufficient image spatial and spectral resolution of the desired reconstruction. Fig. S4 in the supplementary shows an example to test the performance using different spectral ranks to reconstruct the images. The higher spectral ranks can keep more spectral information in the reconstructed images. However, R for the time domain was set to be small, as the cloud shadows were in different positions of the images at different time points. Using the small R can remove the shadow signals from the time domain.

The advantage of using the tensor decomposition is that this method can remove the cloud shadow within or across images. The prerequisite of this method is that images should have significant overlap and the cloud shadow should change with locations inside the image. Compared to other methods using additional sensors e.g. radiometer or LiDAR, this method only requires high overlapping of UAS images so that there is a common area to perform the tensor decomposition. This can be done with repeated flights with UAS. Tucker tensor decomposition can take care of artifacts and image noise simultaneously. For instance, in

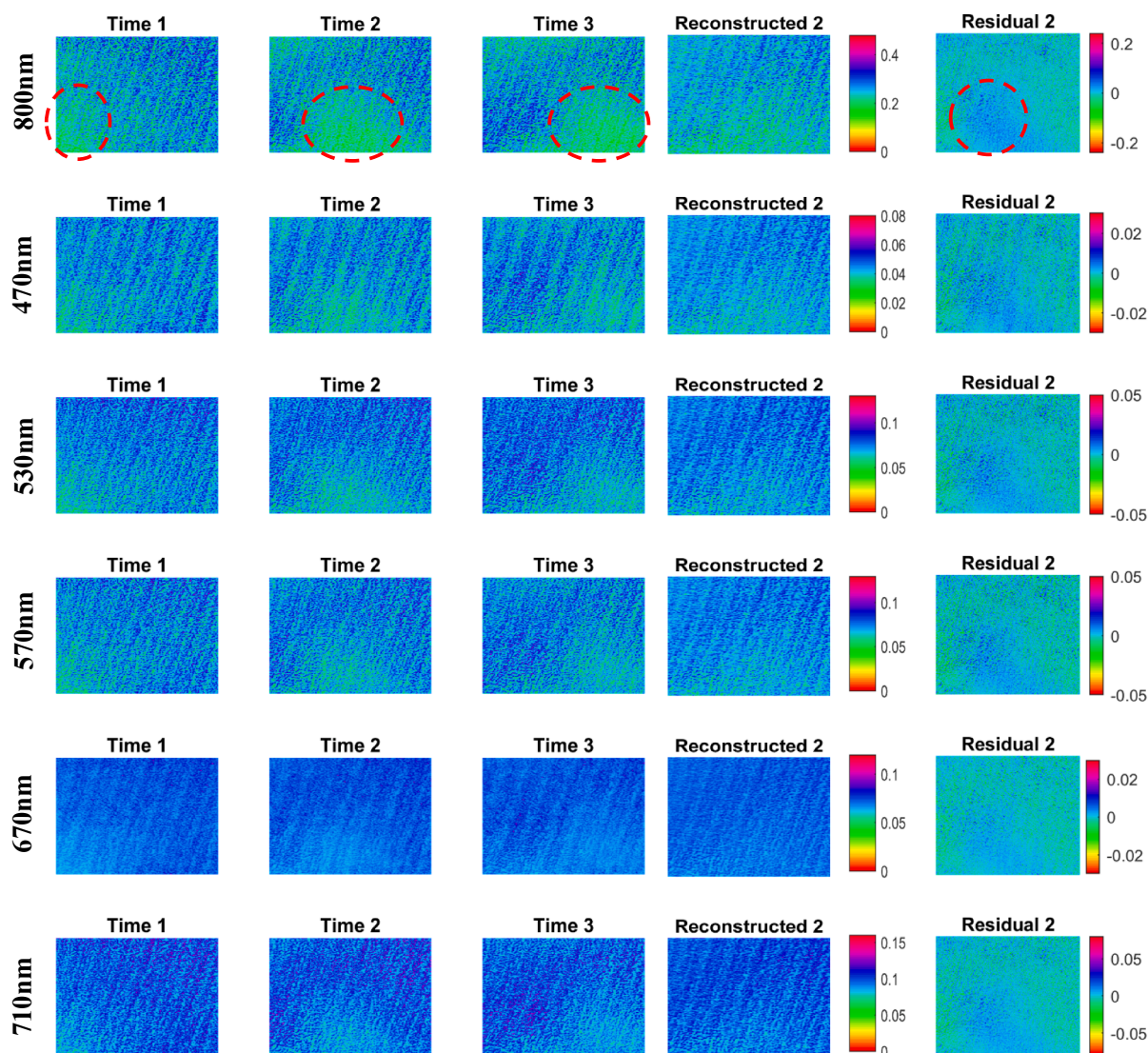


Fig. 11. Cloud shadow removal by the tensor decomposition. Images are reflectance collected from the UAS campaigns at the willow plantation. The areas correspond to the same area shown in Fig. 7. Each panel corresponds to each channel of MCA (800, 470, 530, 570, 670 and 710 nm). The columns represent the image at the time point 1, the time point 2 and the time point 3. The fourth column is the reconstructed image for the time point 2 and the fifth column is the residual (the reconstructed image minus the original image) for the time point 2. To highlight anomalies in the fifth column residual image, the range for the legend of the residual images are half of the range for other column images. The reconstructed images and residuals for the other time points can be found in the supplemental Fig. S2. The circles indicate the location cloud shadow, which is changing with time. We only put circles in the first panel as the location of the cloud shadow is similar in the other panels.

Fig. 11, it can be seen that besides the cloud shadow, there are also residuals for other parts of images. The noise residual may correspond to the image noise. Another advantage of using Tucker for cloud shadow removal is that orthophotos are reconstructed for each time point. This is of particular advantage when time-resolved spatial-temporal patterns are to be investigated. However, with reducing noise on the cloud shadow, this tensor decomposition tends to smooth the imagery and the residuals may contain useful information from the original imagery.

In this study, we also compared the cloud shadow corrected reconstruction of the tensor decomposition and a simple reference method, where a reconstruction could be obtained as the average pixel values over all time points. We found that the simple mean method can achieve a similar but slightly worse result than the tensor decomposition. However, the advantage of using Tucker for cloud shadow

removal compared to a simple temporal mean per pixel is that orthophotos can be reconstructed for each time point and pixel. This is of particular advantage when using remote sensing images acquired across different moments in time where the land surface conditions do vary. Although a simple temporal mean method would remove spatial patterns of images that change over time to some extent, the tensor decomposition could be used to remove artifacts and noise simultaneously (Renard et al., 2006; Zhang et al., 2016).

4.5. Vicarious reflectance validation

Fig. 12 shows the validation of the reflectance obtained from three UAS campaigns. The results indicate that there is a good accuracy for the reflectance with RMSD around 3% compared to handheld radiometer (ASD) reflectance. It should be noticed that the validation is only

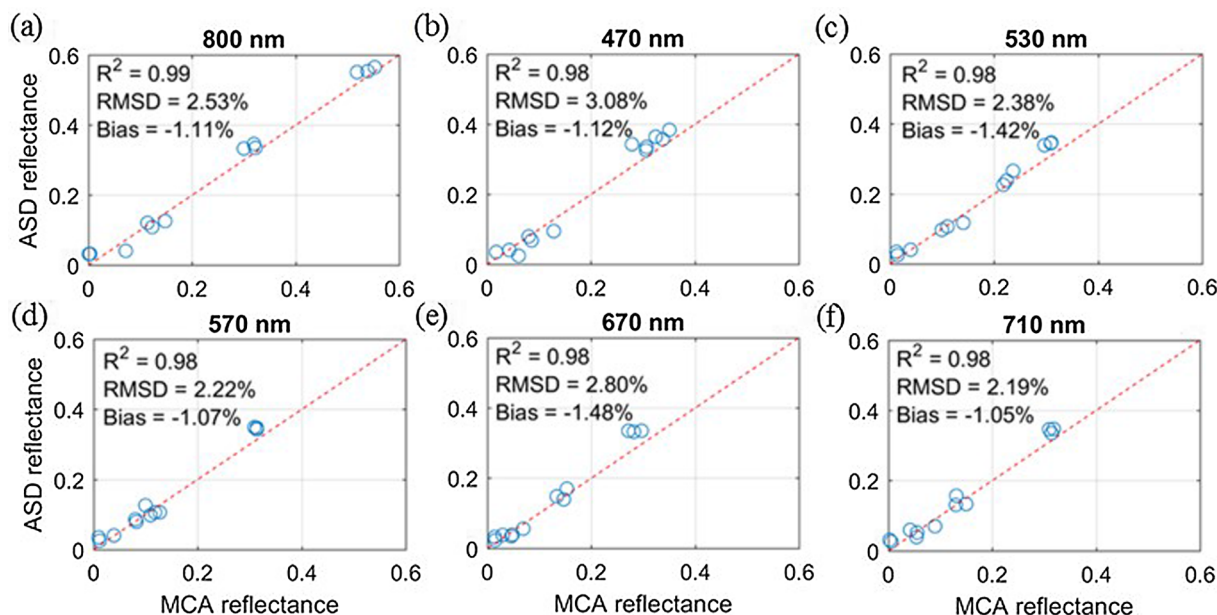


Fig. 12. Validation of reflectance of four color tarpaulins (blue, green, black and silver) collected from MCA at sunny moments with ground ASD measurements during UAS flight campaigns on 19th May, 26th May and 18th June 2017. (For interpretation of the references to color in this figure legend, the reader is referred to the web version of this article.)

for the images collected at sunny moments (not processed by the tensor decomposition). Due to the Rayleigh scattering, the radiance at the sensor is lower than the reflected radiance at the surface. The reflectance from MCA tends to be lower than the reflectance obtained from ASD on the ground. The reflectance can be further improved with the atmospheric correction using the atmospheric radiative transfer modeling approach as Berni et al. (2009) or the empirical line approach (Smith and Milton, 1999) with the reflectance measurements of tarpaulins. Table 4 summarizes the reflectance obtained from other UAS studies. Compare to these studies, this study achieved a comparable accuracy with RMSD of reflectance around 2–3% for high latitude conditions.

5. Conclusion

Quantitative UAS based multispectral remote sensing has great potential in environmental monitoring applications with the advantage over satellites that the imagery can be acquired under overcast conditions. However, most of the optical UAS remote sensing methods have been designed for clear sky conditions or at least uniform irradiance. Unfortunately, such atmospheric conditions are rare in many climate

regions. Particularly, high latitude regions have a high frequency of intermittent clouds together with low illumination conditions. To increase the operational use of UAS multispectral image acquisition under such conditions, we have developed a workflow that improves the sensor sensitivity, accounts for low irradiance and cloud shadows producing orthorectified and radiometrically calibrated multispectral mosaics.

We first proposed a pixel-wise radiometric and geometric calibration that extends the sensor calibration to low illumination conditions ($< 0.3 \text{ W m}^{-2} \text{ sr}^{-1} \text{ nm}^{-1}$) and at the same time corrects vignetting effects. To increase the sensor sensitivity, we used individual settings for each channel, instead of uniform settings, to allow for higher signal-to-noise ratios. We showed that a multivariate method, Tucker tensor decomposition, corrected the reflectance of cloud shadows in multispectral imagery collected on variable irradiance conditions. Finally, a vicarious reflectance validation indicates that the multispectral imagery from UAS campaigns can provide reliable reflectance with root mean square deviations around 2.2–3%.

The issue of frequent and variable cloudy conditions is not only relevant for high latitude regions, e.g. northern Europe, but also for tropical regions, such as Amazonia, central Africa and Southeast Asia

Table 4
Summary of the accuracy of UAS based reflectance.

Sensor	Survey location	Reflectance accuracy	Method	Flight height above the ground (m)	Note	Source
MCA	4.78°W 37.88°N	RMSD 1.17%	Radiance based method	150	Atmospheric correction	Berni et al. (2009)
MCA	116°E 39.3°N	RMSD 2–5%	nonlinear empirical line method	50		Deng et al. (2018a)
MCA	105.96°W 32.89°N	RMSD 1.7–2.2%	Empirical line method	210		Laliberte et al. (2011)
MCA	147.43°E 42.8°S	RMSD 0.025–0.064%	Empirical line method	45		Iqbal et al. (2018)
SONY NEX-7	28.6°E 22.7°S	RMSD 6.3%	Empirical line method	160		Mafanya et al. (2018)
Cubert UHD 185	6.98°E 50.5°N	Errors less than 1%	Empirical line method	30	Hyperspectral	Aasen et al. (2015)
Cubert UHD 185	116°E 39.3°N	Errors less than 3–5%	Empirical line method	50	Hyperspectral	Yang et al. (2017)
Cubert UHD 185	115.83°E 39.45°N	RMSD 3.3–6%	Empirical line method	30–120 m	Hyperspectral	Deng et al. (2018b)
Fabry-Pérot Interferometer (FPI) based camera	35.54E 67.01N	Errors less than 5%	Empirical line method	100	Hyperspectral	Honkavaara and Khoramshahi (2018)

(Asner, 2001). Tucker tensor decomposition methods for cloud shadow removal could be used to efficiently improve current multispectral and hyperspectral image correction techniques for both satellites and UAS.

Acknowledgement

The authors would like to thank the EU and Innovation Fund Denmark (IFD) for funding, in the frame of the collaborative international consortium AgWIT financed under the ERA-NET Co-fund Water Works 2015 Call. This ERA-NET is an integral part of the 2016 Joint Activities developed by the Water Challenges for a Changing World Joint Programme Initiative (Water JPI). This study was also supported by the Smart UAV project from IFD [125-2013-5]. SW acknowledge an internal PhD grant from the Department of Environmental Engineering at DTU and a short-term research stage with PZT financed by the COST action OPTIMISE. The authors would like to thank the editors and two anonymous reviewers for the comments and suggestions to improve the quality of this paper.

Appendix A. Supplementary material

Supplementary data to this article can be found online at <https://doi.org/10.1016/j.isprsjprs.2019.06.017>. These data include Google maps of the most important areas described in this article.

References

- Aasen, H., Burkart, A., Bolten, A., Bareth, G., 2015. Generating 3D hyperspectral information with lightweight UAV snapshot cameras for vegetation monitoring: from camera calibration to quality assurance. *ISPRS J. Photogramm. Remote Sens.* 108, 245–259. <https://doi.org/10.1016/j.isprsjprs.2015.08.002>.
- Aasen, H., Honkavaara, E., Lucieer, A., Zarco-Tejada, P.J., 2018. Quantitative remote sensing at ultra-high resolution with UAV spectroscopy: a review of sensor technology, measurement procedures, and data correction workflows. *Remote Sens.* <https://doi.org/10.3390/rs10071091>.
- Abe, J., Marzolf, I., Ries, J., 2010. Small-format aerial photography. *Small-Format Aer. Photogr.* <https://doi.org/10.1016/C2009-0-18493-3>.
- Adeline, K.R.M., Chen, M., Briottet, X., Pang, S.K., Paparoditis, N., 2013. Shadow detection in very high spatial resolution aerial images: a comparative study. *ISPRS J. Photogramm. Remote Sens.* <https://doi.org/10.1016/j.isprsjprs.2013.02.003>.
- Anderson, K., Gaston, K.J., 2013. Lightweight unmanned aerial vehicles will revolutionize spatial ecology. *Front. Ecol. Environ.* 11, 138–146. <https://doi.org/10.1890/120150>.
- Asner, G.P., 2001. Cloud cover in Landsat observations of the Brazilian Amazon. *Int. J. Remote Sens.* 22, 3855–3862. <https://doi.org/10.1080/01431160010006926>.
- Bandini, F., Lopez-Tamayo, A., Merediz-Alonso, G., Olesen, D., Jakobsen, J., Wang, S., García, M., Bauer-Gottwein, P., 2018. Unmanned aerial vehicle observations of water surface elevation and bathymetry in the cenotes and lagoons of the Yucatan Peninsula. *Mexico. Hydrogeol. J.* 1–16.
- Bendig, J., Yu, K., Aasen, H., Bolten, A., Bennertz, S., Broscheit, J., Gny, M.L., Bareth, G., 2015. Combining UAV-based plant height from crop surface models, visible, and near infrared vegetation indices for biomass monitoring in barley. *Int. J. Appl. Earth Obs. Geoinf.* 39, 79–87. <https://doi.org/10.1016/j.jag.2015.02.012>.
- Berni, J., Zarco-Tejada, P.J., Suarez, L., Fereres, E., 2009. Thermal and narrowband multispectral remote sensing for vegetation monitoring from an unmanned aerial vehicle. *IEEE Trans. Geosci. Remote Sens.* 47, 722–738. <https://doi.org/10.1109/TGRS.2008.2010457>.
- Biggar, S.F., Slater, P.N., Gellman, D.I., 1994. Uncertainties in the in-flight calibration of sensors with reference to measured ground sites in the 0.4–1.1 μm range. *Remote Sens. Environ.* [https://doi.org/10.1016/0034-4257\(94\)90145-7](https://doi.org/10.1016/0034-4257(94)90145-7).
- Brell, M., Segl, K., Guanter, L., Bookhagen, B., 2017. Hyperspectral and Lidar Intensity Data Fusion: A Framework for the Rigorous Correction of Illumination, Anisotropic Effects, and Cross Calibration. *IEEE Trans. Geosci. Remote Sens.* 55, 2799–2810. <https://doi.org/10.1109/TGRS.2017.2654516>.
- Colomina, I., Molina, P., 2014. Unmanned aerial systems for photogrammetry and remote sensing: a review. *ISPRS J. Photogramm. Remote Sens.* 92, 79–97. <https://doi.org/10.1016/j.isprsjprs.2014.02.013>.
- Del Pozo, S., Rodríguez-González, P., Hernández-López, D., Felipe-García, B., 2014. Vicarious radiometric calibration of a multispectral camera on board an unmanned aerial system. *Remote Sens.* 6, 1918–1937. <https://doi.org/10.3390/rs6031918>.
- Deng, L., Mao, Z., Li, X., Hu, Z., Duan, F., Yan, Y., 2018a. UAV-based multispectral remote sensing for precision agriculture: a comparison between different cameras. *ISPRS J. Photogramm. Remote Sens.* <https://doi.org/10.1016/j.isprsjprs.2018.09.008>.
- Deng, L., Yan, Y., Gong, H., Duan, F., Zhong, R., 2018b. The effect of spatial resolution on radiometric and geometric performances of a UAV-mounted hyperspectral 2D imager. *ISPRS J. Photogramm. Remote Sens.* <https://doi.org/10.1016/j.isprsjprs.2018.08.002>.
- Ferrero, A., Campos, J., Pons, A., 2006. Low-uncertainty absolute radiometric calibration of a CCD. *Metrologia.* <https://doi.org/10.1088/0026-1394/43/2/S04>.
- Fytisilis, A.L., Prokoss, A., Koutroubas, K.D., Michail, D., Kontoes, C.C., 2016. A methodology for near real-time change detection between Unmanned Aerial Vehicle and wide area satellite images. *ISPRS J. Photogramm. Remote Sens.* 119, 165–186. <https://doi.org/10.1016/j.isprsjprs.2016.06.001>.
- Hakala, T., Honkavaara, E., Saari, H., Mäkyinen, J., Kaivosoja, J., Pesonen, L., Pölonen, I., 2013. Spectral imaging from Uavs under varying illumination conditions. *ISPRS - Int. Arch. Photogramm. Remote Sens. Spat. Inf. Sci. XI-1/W2*, 189–194. <https://doi.org/10.5194/isprsarchives-XI-1-W2-189-2013>.
- Hakala, T., Suomalainen, J., Peltoniemi, J.I., 2010. Acquisition of bidirectional reflectance factor dataset using a micro unmanned aerial vehicle and a consumer camera. *Remote Sens.* 2, 819–832. <https://doi.org/10.3390/rs2030819>.
- Honkavaara, E., Arbiol, R., Markelin, L., Martinez, L., Cramer, M., Bovet, S., Chandelier, L., Iives, R., Klonus, S., Marshal, P., Schläpfer, D., Tabor, M., Thom, C., Veje, N., 2009. Digital airborne photogrammetry—a new tool for quantitative remote sensing?—a state-of-the-art review on radiometric aspects of digital photogrammetric images. *Remote Sens.* 1, 577–605. <https://doi.org/10.3390/rs1030577>.
- Honkavaara, E., Khoramshahi, E., 2018. Radiometric correction of close-range spectral image blocks captured using an unmanned aerial vehicle with a radiometric block adjustment. *Remote Sens.* <https://doi.org/10.3390/rs10020256>.
- Honkavaara, E., Markelin, L., Rosnell, T., Nurminen, K., 2012. Influence of solar elevation in radiometric and geometric performance of multispectral photogrammetry. *ISPRS J. Photogramm. Remote Sens.* 67, 13–26. <https://doi.org/10.1016/j.isprsjprs.2011.10.001>.
- Honkavaara, E., Saari, H., Kaivosoja, J., Pölonen, I., Hakala, T., Litkey, P., Mäkyinen, J., Pesonen, L., 2013. Processing and assessment of spectrometric, stereoscopic imagery collected using a lightweight UAV spectral camera for precision agriculture. *Remote Sens.* 5, 5006–5039. <https://doi.org/10.3390/rs5105006>.
- Iqbal, F., Lucieer, A., Barry, K., 2018. Simplified radiometric calibration for UAS-mounted multispectral sensor. *Eur. J. Remote Sens.* <https://doi.org/10.1080/22797254.2018.1432293>.
- Kanniah, K.D., Beringer, J., North, P., Hutley, L., 2012. Control of atmospheric particles on diffuse radiation and terrestrial plant productivity: a review. *Prog. Phys. Geogr.* 36, 209–237. <https://doi.org/10.1177/0309133311434244>.
- Keley, J., Lucieer, A., 2012. Sensor correction of a 6-band multispectral imaging sensor for UAV remote sensing. *Remote Sens.* 4, 1462–1493. <https://doi.org/10.3390/rs4051462>.
- Korpela, I., Heikkinen, V., Honkavaara, E., Rohrbach, F., Tokola, T., 2011. Variation and directional anisotropy of reflectance at the crown scale - implications for tree species classification in digital aerial images. *Remote Sens. Environ.* 115, 2062–2074. <https://doi.org/10.1016/j.rse.2011.04.008>.
- Laliberte, A.S., Goforth, M.A., Steele, C.M., Rango, A., 2011. Multispectral remote sensing from unmanned aircraft: image processing workflows and applications for rangeland environments. *Remote Sens.* 3, 2529–2551. <https://doi.org/10.3390/rs3112529>.
- Li, X., Wang, L., Cheng, Q., Wu, P., Gan, W., Fang, L., 2019a. Cloud removal in remote sensing images using nonnegative matrix factorization and error correction. *ISPRS J. Photogramm. Remote Sens.* <https://doi.org/10.1016/j.isprsjprs.2018.12.013>.
- Li, Z., Shen, H., Cheng, Q., Liu, Y., You, S., He, Z., 2019b. Deep learning based cloud detection for medium and high resolution remote sensing images of different sensors. *ISPRS J. Photogramm. Remote Sens.* <https://doi.org/10.1016/j.isprsjprs.2019.02.017>.
- Lowe, D.G., 2004. Distinctive image features from scale-invariant keypoints. *Int. J. Comput. Vis.* 60, 91–110. <https://doi.org/10.1023/B:VISI.0000029664.99615.94>.
- Mafanya, M., Tsele, P., Botai, J.O., Manyama, P., Chirima, G.J., Monate, T., 2018. Radiometric calibration framework for ultra-high-resolution UAV-derived orthomosaics for large-scale mapping of invasive alien plants in semi-arid woodlands: *Harrisia pomaniensis* as a case study. *Int. J. Remote Sens.* <https://doi.org/10.1080/01431161.2018.1490503>.
- Manfreda, S., McCabe, M.F., Miller, P.E., Lucas, R., Madrigal, V.P., Mallinis, G., Dor, E.B., Helman, D., Estes, L., Ciruolo, G., Müllerová, J., Tauro, F., de Lima, M.I., de Lima, J.L.M.P., Maltese, A., Frances, F., Caylor, K., Kohv, M., Perks, M., Ruiz-Pérez, G., Su, Z., Vico, G., Toth, B., 2018. On the use of unmanned aerial systems for environmental monitoring. *Remote Sens.* 10, 641. <https://doi.org/10.3390/rs10040641>.
- McCabe, M.F., Rodell, M., Alsdorf, D.E., Miralles, D.G., Uijlenhoet, R., Wagner, W., Lucieer, A., Houborg, R., Verhoest, N.E.C., Franz, T.E., Shi, J., Gao, H., Wood, E.F., 2017. The future of Earth observation in hydrology. *Hydrol. Earth Syst. Sci.* 21, 3879–3914. <https://doi.org/10.5194/hess-21-3879-2017>.
- Mesas-Carrascosa, F.J., Clavero Rumbao, I., Torres-Sánchez, J., García-Ferrer, A., Peña, J.M., López Granados, F., 2017. Accurate ortho-mosaicked six-band multispectral UAV images as affected by mission planning for precision agriculture proposes. *Int. J. Remote Sens.* 38, 2161–2176. <https://doi.org/10.1080/01431161.2016.1249311>.
- Mørup, M., 2011. Applications of tensor (multiway array) factorizations and decompositions in data mining. *Wiley Interdiscip. Rev. Data Min. Knowl. Discov.* 1, 24–40. <https://doi.org/10.1002/widm.1>.
- Renard, N., Bourennane, S., Blanc-Talon, J., 2006. Robust target detection by spatial/spectral restoration based on tensor modelling. *Int. Proceedings - International Conference on Image Processing. ICIP.* <https://doi.org/10.1109/ICIP.2007.4379351>.
- Schirmann, M., Giebel, A., Gleiniger, F., Pflanz, M., Lentschke, J., Dammer, K.-H., 2016. Monitoring agronomic parameters of winter wheat crops with low-cost UAV imagery. *Remote Sens.* 8, 706. <https://doi.org/10.3390/rs8090706>.
- Schläpfer, D., Richter, R., Kellenberger, T., 2012. Atmospheric and Topographic Correction of Photogrammetric Airborne Digital Scanner Data (Atcor-Ads). *EuroSDR - EUROCOV 2012*.
- Smith, G.M., Milton, E.J., 1999. The use of the empirical line method to calibrate remotely sensed data to reflectance. *Int. J. Remote Sens.* 20, 2653–2662. <https://doi.org/10.1080/014311699211994>.

- Turner, D., Lucieer, A., Malenovský, Z., King, D., Robinson, S., 2014. Spatial co-registration of ultra-high resolution visible, multispectral and thermal images acquired with a micro-UAV over antarctic moss beds. *Remote Sens.* 6, 4003–4024. <https://doi.org/10.3390/rs6054003>.
- Von Bueren, S.K., Burkart, A., Hueni, A., Rascher, U., Tuohy, M.P., Yule, I.J., 2015. Deploying four optical UAV-based sensors over grassland: challenges and limitations. *Biogeosciences* 12, 163–175. <https://doi.org/10.5194/bg-12-163-2015>.
- Wang, S., Garcia, M., Bauer-Gottwein, P., Jakobsen, J., Zarco-Tejada, P.J., Bandini, F., Paz, V.S., Ibrom, A., 2019. High spatial resolution monitoring land surface energy, water and CO2 fluxes from an Unmanned Aerial System. *Remote Sens. Environ.* 229, 14–31. <https://doi.org/10.1016/j.rse.2019.03.040>.
- Wang, S., Ibrom, A., Bauer-Gottwein, P., Garcia, M., 2018. Incorporating diffuse radiation into a light use efficiency and evapotranspiration model: an 11-year study in a high latitude deciduous forest. *Agric. For. Meteorol.* 248, 479–493. <https://doi.org/10.1016/j.agrformet.2017.10.023>.
- Westoby, M.J., Brasington, J., Glasser, N.F., Hambrey, M.J., Reynolds, J.M., 2012. “Structure-from-Motion” photogrammetry: a low-cost, effective tool for geoscience applications. *Geomorphology* 179, 300–314. <https://doi.org/10.1016/j.geomorph.2012.08.021>.
- Yang, G., Li, C., Wang, Y., Yuan, H., Feng, H., Xu, B., Yang, X., 2017. The DOM generation and precise radiometric calibration of a UAV-mounted miniature snapshot hyperspectral imager. *Remote Sens.* <https://doi.org/10.3390/rs9070642>.
- Yu, W., 2004. Practical anti-vignetting methods for digital cameras. *IEEE Trans. Consum. Electron.* 50, 975–983. <https://doi.org/10.1109/TCE.2004.1362487>.
- Yu, X., Liu, Q., Liu, X., Liu, Xiangyang, Wang, Y., 2016. A physical-based atmospheric correction algorithm of unmanned aerial vehicles images and its utility analysis. *Int. J. Remote Sens.* 1–12. <https://doi.org/10.1080/01431161.2016.1230291>.
- Zarco-Tejada, P.J., González-Dugo, V., Berni, J.A.J., 2012. Fluorescence, temperature and narrow-band indices acquired from a UAV platform for water stress detection using a micro-hyperspectral imager and a thermal camera. *Remote Sens. Environ.* 117, 322–337. <https://doi.org/10.1016/j.rse.2011.10.007>.
- Zhai, H., Zhang, H., Zhang, L., Li, P., 2018. Cloud/shadow detection based on spectral indices for multi/hyperspectral optical remote sensing imagery. *ISPRS J. Photogramm. Remote Sens.* <https://doi.org/10.1016/j.isprsjprs.2018.07.006>.
- Zhang, Liangpei, Zhang, Lefei, Tao, D., Huang, X., 2013. Tensor discriminative locality alignment for hyperspectral image spectral-spatial feature extraction. *IEEE Trans. Geosci. Remote Sens.* 51, 242–256. <https://doi.org/10.1109/TGRS.2012.2197860>.
- Zhang, X., Wen, G., Dai, W., 2016. A tensor decomposition-based anomaly detection algorithm for hyperspectral image. *IEEE Trans. Geosci. Remote Sens.* 54, 5801–5820. <https://doi.org/10.1109/TGRS.2016.2572400>.
- Zheng, Y., Lin, S., Kang, S.B., Xiao, R., Gee, J.C., Kambhamettu, C., 2013. Single-image vignetting correction from gradient distribution symmetries. *IEEE Trans. Pattern Anal. Mach. Intell.* 35, 1480–1494. <https://doi.org/10.1109/TPAMI.2012.210>.